

## Article

# Cysteine-Induced Hybridization of 2D Molybdenum Disulfide Films for Efficient and Stable Hydrogen Evolution Reaction

Arunas Jagminas <sup>1,\*</sup>, Paulius Gaigalas <sup>1</sup>, Carla Bittencourt <sup>2</sup>  and Vaclovas Klimas <sup>1</sup> 

<sup>1</sup> The Department of Electrochemical Materials Science, State Research Institute Center for Physical Sciences and Technology, Sauletekio ave. 3, LT-01257 Vilnius, Lithuania; paulius.gaigalas@ftmc.lt (P.G.); vaclovas.klimas@ftmc.lt (V.K.)

<sup>2</sup> Chimie des Interactions Plasma-Surface, University of Mons, Place du Parc 22, 7000 Mons, Belgium; Carla.BITTENCOURT@umons.ac.be

\* Correspondence: arunas.jagminas@ftmc.lt

**Abstract:** The noble, metal-free materials capable of efficiently catalyzing water splitting reactions currently hold a great deal of promise. In this study, we reported the structure and electrochemical performance of new MoS<sub>2</sub>-based material synthesized with L-cysteine. For this, a facile one-pot hydrothermal process was developed and an array of densely packed nanoplatelet-shaped hybrid species directly on a conductive substrate were obtained. The crucial role of L-cysteine was determined by numerous methods on the structure and composition of the synthesized material and its activity and stability for hydrogen evolution reaction (HER) from the acidic water. A low Tafel slope of 32.6 mV dec<sup>-1</sup>, close to a Pt cathode, was registered for the first time. The unique HER performance at the surface of this hybrid material in comparison with recently reported MoS<sub>2</sub>-based electrocatalysts was attributed to the formation of more defective 1T, 2H-MoS<sub>2</sub>/MoO<sub>x</sub>, C nanostructures with the dominant 1T-MoS<sub>2</sub> phase and thermally degraded cysteine residues entrapped. Numerous stacks of metallic (1T-MoS<sub>2</sub> and MoO<sub>2</sub>) and semiconducting (2H-MoS<sub>2</sub> and MoO<sub>3</sub>) fragments relayed the formation of highly active layered nanosheets possessing a low hydrogen adsorption free energy and much greater durability, whereas intercalated cysteine fragments had a low Tafel slope of the HER reaction. X-ray photoelectron spectroscopy, scanning electron microscopy, thermography with mass spectrometry, high-resolution transmission electron microscopy, Raman spectroscopy techniques, and linear sweep voltammetry were applied to verify our findings.

**Keywords:** molybdenum disulfide; L-cysteine; hydrothermal synthesis; hybrid films; electrocatalyst; water splitting



**Citation:** Jagminas, A.; Gaigalas, P.; Bittencourt, C.; Klimas, V. Cysteine-Induced Hybridization of 2D Molybdenum Disulfide Films for Efficient and Stable Hydrogen Evolution Reaction. *Materials* **2021**, *14*, 1165. <https://doi.org/10.3390/ma14051165>

Academic Editor: Haralampos N. Miras

Received: 1 February 2021

Accepted: 24 February 2021

Published: 2 March 2021

**Publisher's Note:** MDPI stays neutral with regard to jurisdictional claims in published maps and institutional affiliations.



**Copyright:** © 2021 by the authors. Licensee MDPI, Basel, Switzerland. This article is an open access article distributed under the terms and conditions of the Creative Commons Attribution (CC BY) license (<https://creativecommons.org/licenses/by/4.0/>).

## 1. Introduction

Hydrogen gas produced from water electrolysis via catalytic splitting is ascribed to a mostly clean energy carrier. However, to achieve relevance for practical usage, the hydrogen evolution reaction (HER) rate, as at the surface of a Pt-based electrode, which exhibits the best HER performance [1], requires alternative cheaper catalysts.

Over the past decade, numerous reports have been devoted to the synthesis of various nanostructured materials for catalysis of water splitting reactions. Among them, nanoscale MoS<sub>2</sub> species have been the most intensively investigated 2D material because of the specific graphene-like layered morphology and unique catalytic, biological, and energy-related properties [2–5]. However, the intrinsic conductivity, catalytic activity, and stability of the pure and the most thermodynamically stable 2H-MoS<sub>2</sub> nanostructured films are usually poor in comparison with Pt group metals and compounds [6]. In addition, the overvoltage of pristine 2H-MoS<sub>2</sub> nanoplatelets for HER is significantly larger, about −0.2 V vs. reference hydrogen electrode, RHE, potential [7–10] compared with Pt/C [7]. Therefore, much effort has been devoted to the development of novel, more effective hybrid electrocatalysts. In this context, MoS<sub>2</sub> films doped by other elements [11]; hybridized with 1T-MoS<sub>2</sub> [12,13],

WO<sub>3</sub> [14], and glycine [15]; decorated with various guest nanoparticles [16–18]; deposited onto graphite [19], graphene, and graphene oxides [20,21]; and carbon nanotubes [22] have been proposed. Various methods have been explored to synthesize layered MoS<sub>2</sub> nanomaterials, including laser ablation [23], thermal decomposition [24], gas-phase reaction [25], magnetron sputtering [26], and hydrothermal [27] or sonochemical [28] processing. An efficient strategy to enhance HER activity of MoS<sub>2</sub>-based electrocatalysts is to design highly conductive substrates, such as 3D-structured graphene [29,30], graphene oxide [31], foams [32,33], carbon fiber [34], etc. [22]. Various HER reaction Tafel slopes from 41 to 68 mV dec<sup>-1</sup> and overpotentials from –185 to –260 mV were reported for the best samples. As is known, better HER performance is characteristic for the metastable 1T (1T') phase compared with 2H-MoS<sub>2</sub> atoms and the transformation to the stable 2H-MoS<sub>2</sub> phase. It is crucial to synthesize stable 1T (1T')-MoS<sub>2</sub>-based catalysts [35,36].

It has been both experimentally and theoretically proven that the catalytically active sites for HER are located just at the unsaturated sulfur atoms of the MoS<sub>2</sub> nanoplatelet edges because the edge sites in 2D MoS<sub>2</sub> have near-zero hydrogen absorption free energy (0.08 eV) [37,38]. Consequently, the engineering of defect-rich MoS<sub>2</sub> nanostructures directly influence the activity of MoS<sub>2</sub>-based electrocatalysts the most. Therefore, various post-treatment methods resulting in the design of highly-defective MoS<sub>2</sub> through etching [39], doping [40,41], intercalation [42], and nanoparticulation [36] have been reported. However, the hybridization of MoS<sub>2</sub> nanostructures with cysteine amino acid resulting in the formation of an HER electrocatalyst with a surprisingly low Tafel slope of 32.6 mV dec<sup>-1</sup>, which is the lowest among the reported for MoS<sub>2</sub> materials, has not yet been reported.

Here, we reported the synthesis recipe, chemical composition, structure, and electrochemical performance of a new hybrid material composed of the dominant 1T-MoS<sub>2</sub> phase heterostructured with 2H-MoS<sub>2</sub>, Mo(IV), and Mo(VI) oxide fragments and carbon. We showed that the engineered hybrids have enhanced electrochemical performance and significantly higher stability in comparison with pure 2D MoS<sub>2</sub>, as exhibited by an increase in the HER current density to over 80 mA cm<sup>-2</sup> at –0.35 V overvoltage.

The samples were characterized by means of X-ray photoelectron spectroscopy (XPS), X-ray diffraction (XRD), scanning electron microscopy (SEM), high-resolution transmission electron microscopy (HRTEM), thermogravimetry (TG), and differential thermal spectroscopy (DTA) coupled with mass spectrometry, Raman spectroscopy, and cycling voltammetry.

## 2. Results and Discussion

Hydrothermal processing of the ammonium heptamolybdate and the thiourea solution at 220–225 °C resulted in the formation of crystalline MoS<sub>2</sub> nanoplatelet species in the solution bulk [15]. In this way, uniform and well-attached nanoplatelet films can also be engineered directly at various substrates. The thickness, varying from 0.7 to 2.5 μm, of these black-colored films is mainly dependent on the autoclaving time [15]. The morphology of films formed under the same autoclaving conditions in the solution without and containing L-cysteine was quite similar (Figure 1a).

The HRTEM image (Figure 1b) clearly revealed that the atomic flatness of the sandwiched layers in the composite MoS<sub>2</sub>-cyst film was greatly disrupted because of a non-periodic atom arrangement and increased to 8.4 Å distance between S-Mo-S lattices compared with the characteristic one of crystalline molybdenite 2H-MoS<sub>2</sub> (6.15 Å) [43]. However, a markedly larger variation in the Mo-to-Mo spacing, nonlinear atom distributions, and the presence of numerous twists can be viewed. In many sites, the spacing between neighboring monolayers exceeded 10 Å. According to previous reports, significantly larger distances between the stacked S-Mo-S planes compared with characteristic of pure molybdenite were found, which implied the intercalation of guest molecules.

To further study the intercalation of cysteine or thiourea molecules or fragments inside the film, Raman spectroscopy investigations were performed. Figure 2a displays the Raman spectra of the films designed at the Ti/TiO<sub>2</sub> substrate by hydrothermal synthesis in the basic.

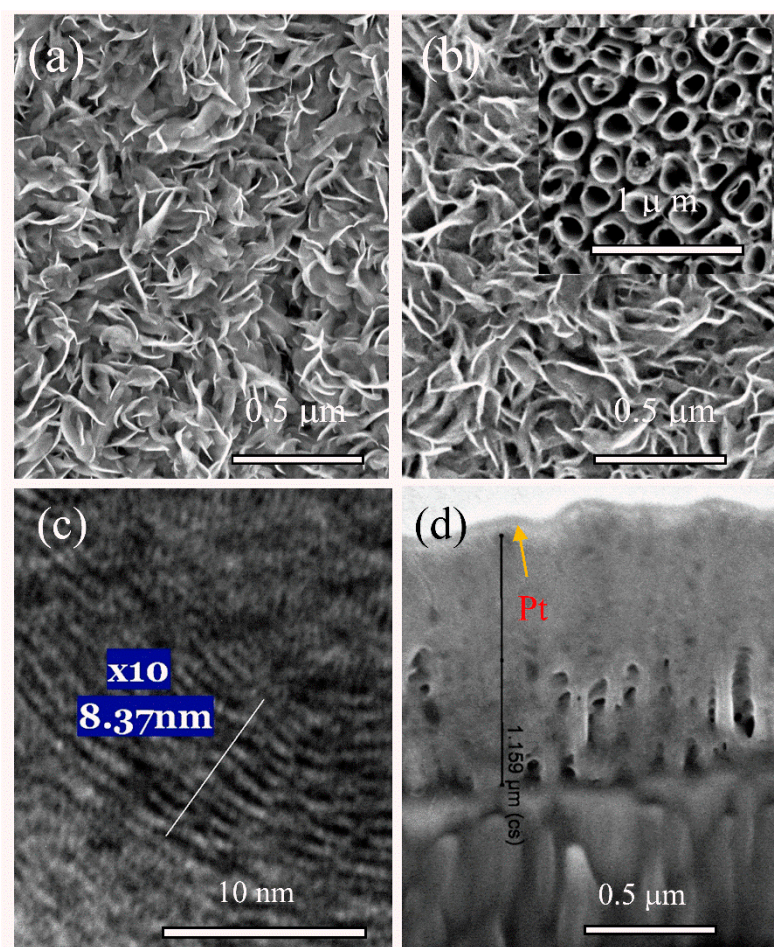


**Figure 1.** Top-side (a,b) and cross-sectional (d) scanning electron microscopy (SEM) and high-resolution transmission electron microscopy (HRTEM) (c) images of film synthesized hydrothermally on the natotubed titania surface (inset) from the solution containing 5.0  $(\text{NH}_4)_6\text{Mo}_7\text{O}_{24} \cdot 4\text{H}_2\text{O}$ , 90 thiourea without (a) and containing 2.0  $\text{mmol L}^{-1}$  L-cysteine (b–d) at 220 °C for 5 h.

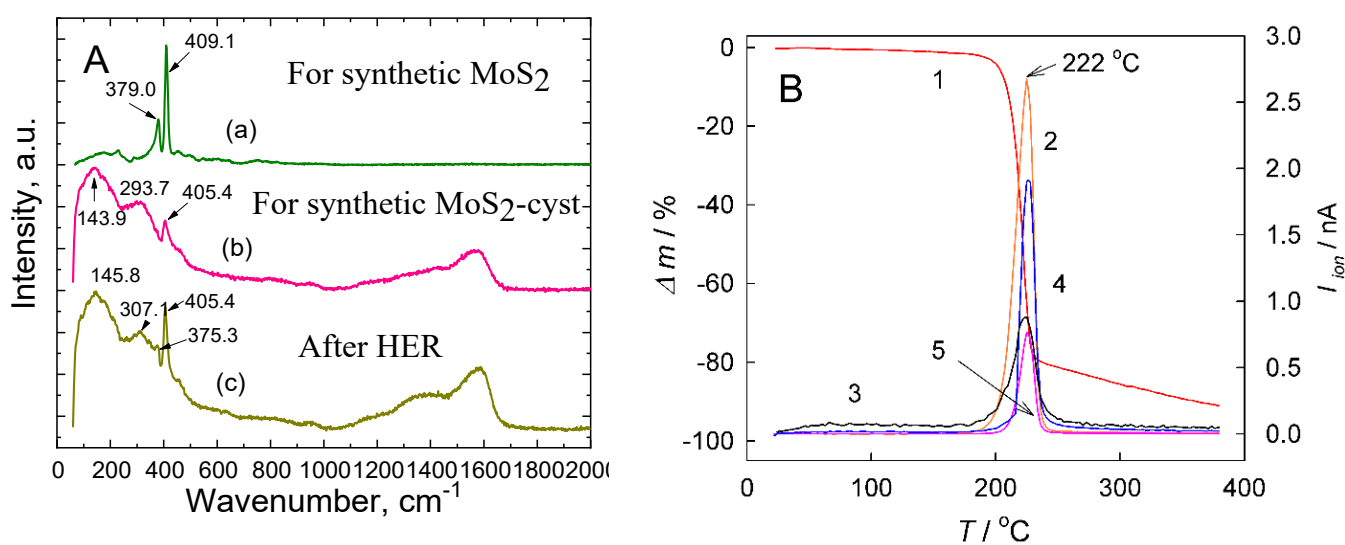


**Figure 2.** (A) Raman spectra of (a) as-grown MoS<sub>2</sub> and (b) MoS<sub>2</sub>-cys films at the Ti/TiO<sub>2</sub> substrate as well as (c) the same MoS<sub>2</sub>-cys film after the HER processing by potential cycling within a range of 0.05 to −0.35 V vs. the RHE potential for 1000 scans; (B) (1) thermogravimetry (TG) plot and variables of (2) CO<sub>2</sub>, (3) H<sub>2</sub>O, (4) NH<sub>3</sub>, and (5) H<sub>2</sub>S ionic currents during annealing of L-cysteine in argon determined by mass spectrometry (MS) analysis.

Solution without (a) and with 2 mmol L<sup>-1</sup> L-cysteine (b,c) before (a,b) and after (c) the prolonged HER processing. As for film synthesized without cysteine, two clearly resolved peaks at 409.1 cm<sup>-1</sup> and 379.0 cm<sup>-1</sup>, attributable to the A<sub>1g</sub> and E<sub>2g</sub><sup>1</sup> longitudinal acoustic phonon modes, respectively, and typical for the crystalline 2H-MoS<sub>2</sub> [20] from few-layered flakes, were detected. The Raman spectrum of the as-grown MoS<sub>2</sub>-cyst film is shown in Figure 2a,b. This spectrum apart of a low intensity A<sub>1g</sub> mode peaked at 405.4 cm<sup>-1</sup>. The broad additional vibration modes peaked at 143.9 and 293.7 cm<sup>-1</sup> and the very broad mode peaked in the 1100–1650 cm<sup>-1</sup> region. These modes can be associated with the presence of molybdenum oxides and organic molecule fragments, respectively, entrapped inside this film [44].

A similar shape of the Raman spectrum is also characteristic for MoS<sub>2</sub>-cys film after the prolonged usage as an HER catalyst by 1000 potential scans within a 0.05 to -0.35 V window (Figure 2a). However, for this film, a significantly sharper and stronger A<sub>1g</sub> mode was determined, likely indicating the presence of a larger amount of crystalline MoS<sub>2</sub> phase compared with the as-grown film.

Identification of gaseous species with  $m/z = 44$  (CO<sub>2</sub>),  $m/z = 17$  (NH<sub>3</sub>), and  $m/z = 34$  (H<sub>2</sub>S) released during the thermal decomposition of cysteine in an argon atmosphere via evolved gas analytical mass spectrometry revealed that all functional groups, namely -COOH, -SH, and -NH<sub>2</sub> ought to be detached from the cysteine molecule at around 220 °C (Figure 2b). Therefore, it was difficult to suspect the intercalation or adsorption of cysteine molecules inside and onto the 2D MoS<sub>2</sub> nanoflakes. This allowed us to draw the important conclusion that an increased HER performance at the hybrid MoS<sub>2</sub>-cyst electrocatalyst cannot be related to adsorption and intercalation of cysteine molecules; from the DTA/MS analysis of all emitted species as well as the XPS data, it could have been COS or CS<sub>2</sub> species formed via the thermal splitting of thiourea and cysteine in a synthesis reactor.

To evaluate the electrolytic HER activity, we performed linear sweep voltammetry (LSV) measurements in a typical three-electrode setup. To assess the durability of the hybrid electrocatalyst, up to 2000 potential sweeps were conducted. Figure 3 shows the sets of LSV curves obtained.

At a potential scan rate of 10 mV s<sup>-1</sup> in argon-saturated 0.5 mol L<sup>-1</sup> H<sub>2</sub>SO<sub>4</sub> solution (pH = 0), films were synthesized without (a) and with L-cysteine (b,c). From these, the onset potential of HER at the cysteine-free as well as the cysteine-used MoS<sub>2</sub> electrode approximated to about -0.2 V vs. RHE. Additionally, from the current density variables, only some higher activity within all tested potential window were obtained for electrodes fabricated using L-cysteine. However, the electrochemical performance of HER at the electrodes grown in the L-cysteine-containing reactor differed significantly. The potential cycling within the 0.05 to -0.35 V potentials window of the L-cysteine-free electrode usually resulted in an HER-activity decrease down to 15–18 mA cm<sup>-2</sup> just after 250 cycles (Figure 3a), implying about a 70% decay from initial activity. In contrast, the electrodes covered with nanoplatelet-shaped hybrid MoS<sub>2</sub>/cysteine film showed considerable higher HER activity in the same potentials window, decreasing insignificantly during the subsequent 2000 potential scans (Figure 3b,c). A further benefit is that MoS<sub>2</sub>/cysteine hybrid HER electrocatalyst possessed significantly lower Tafel slopes (Figure 3b,c) compared with the ones synthesized under the same conditions without cysteine. In the case of films synthesized in the presence of just 1 mmol L<sup>-1</sup> cysteine, the prolonged HER processing resulted in the marked decrease in the Tafel slope value from 57.8 to 40.2 mV dec<sup>-1</sup>, ca. by 30% (Figure 3b). An increase in the cysteine concentration to 3 mmol L<sup>-1</sup> resulted in the surprisingly low Tafel slope value (32.6 mV dec<sup>-1</sup>) of as-grown film, which was the lowest among all reported data for MoS<sub>2</sub>-based electrocatalysts and was close to the Tafel slope value characteristic for the HER at the Pt and Pt/C substrates. The Tafel slope value of 30 mV dec<sup>-1</sup> indicates that the recombination reaction  $H_{ads} + H_{ads} \rightarrow H_2$  is an HER rate-limiting stage followed by a fast discharge reaction:  $H_3O^+ + e \rightarrow H_{ads} + H_2O$ , whereas the Tafel slopes of 40 mV dec<sup>-1</sup> indicates that H<sub>2</sub> evolution proceeds via a Volmer–Heyrovsky pathway [45].

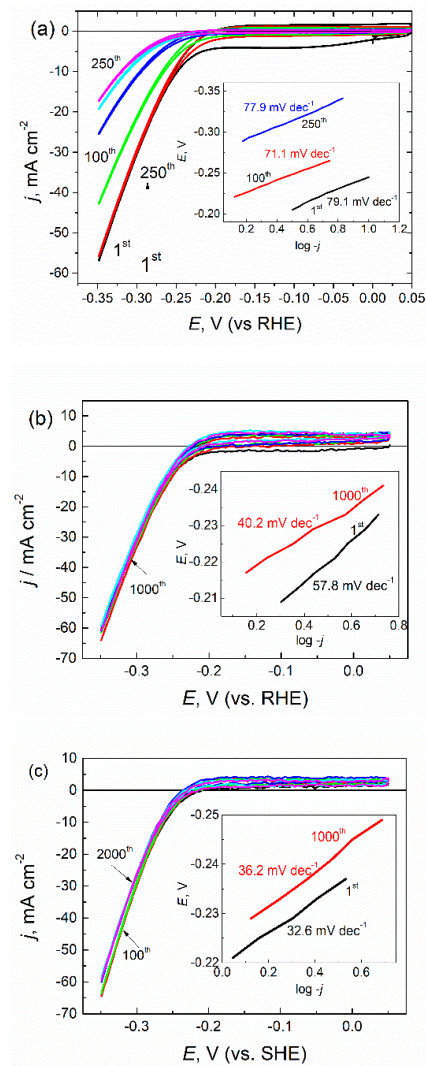


**Figure 3.** The sets of cyclic voltammograms recorded in the  $\text{H}_2$ -saturated solution of  $0.5 \text{ mol L}^{-1} \text{H}_2\text{SO}_4$  at a  $10 \text{ mV s}^{-1}$  potential sweep rate of: (a) pure  $\text{MoS}_2$  film and the same film hybridized with (b) 1.0 and (c) 3.0  $\text{mmol L}^{-1}$  of L-cysteine. In the insets are the Tafel slopes calculated for the indicated specimen and the potential scan cycle.

X-ray photoelectron spectroscopy was used to investigate the chemical states of the elements in the surface region of the synthesized films. The full-range survey spectrum taken from the  $\text{MoS}_2$ -cyst sample is shown in Figure 4a, from which the presence of the Mo, S, O, N, and C elements was evidenced.

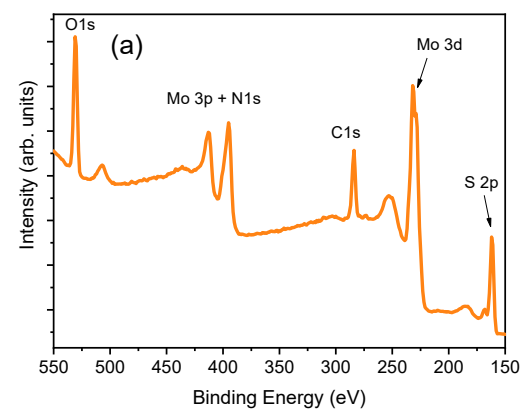


**Figure 4.** Cont.

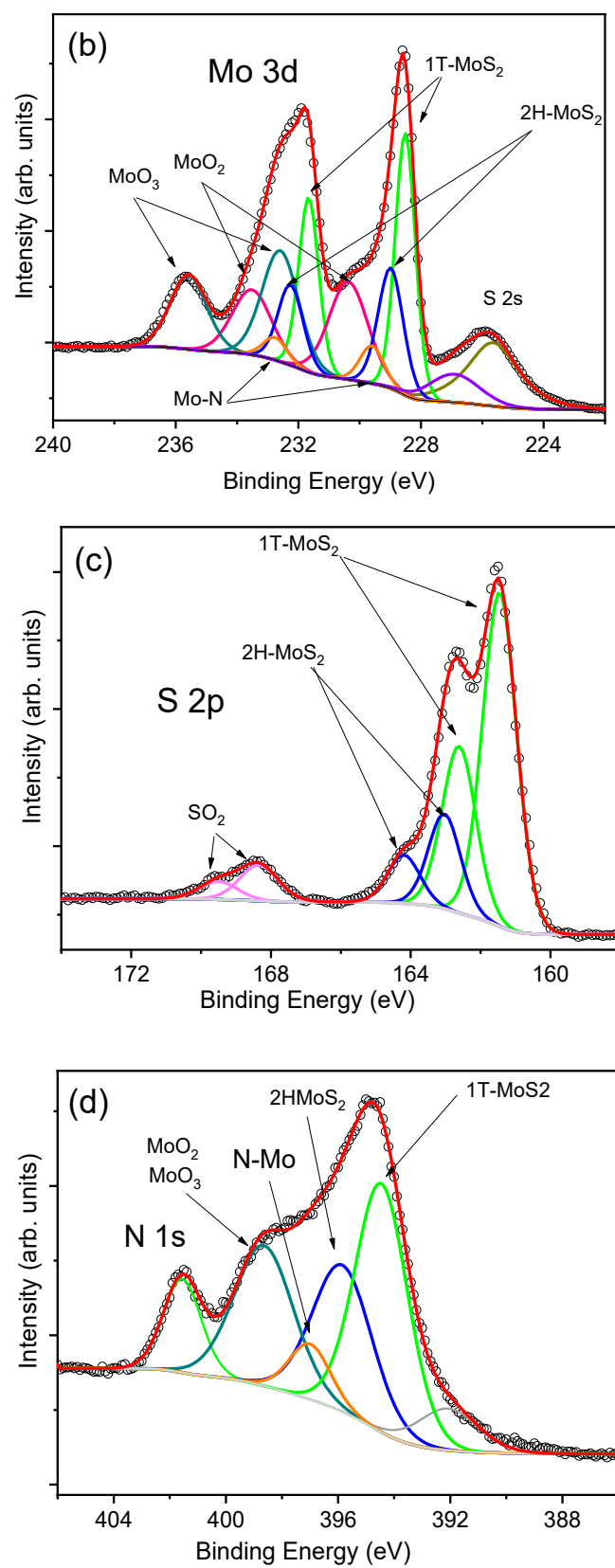
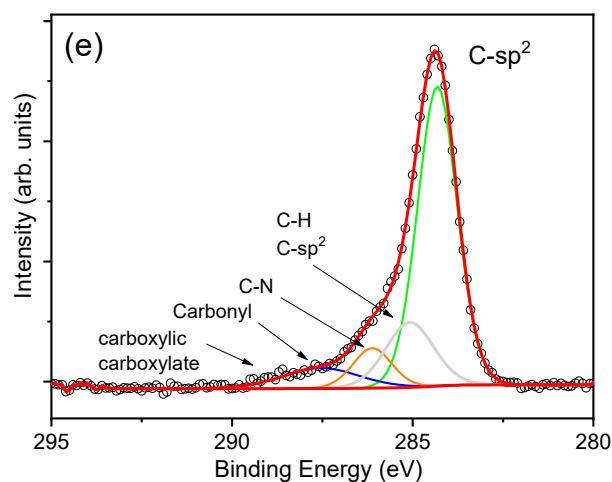


Figure 4. Cont.



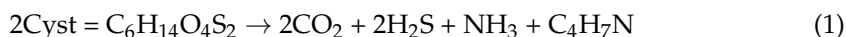
**Figure 4.** X-ray photoelectron spectroscopy (XPS) spectra of as-grown MoS<sub>2</sub>-cyst film: (a): survey, (b): Mo 3d, (c): S 2p, (d): Mo 3p, and (e): C 1s.

Figure 4b revealed the presence of Mo<sup>4+</sup> in both the semiconducting 2H-MoS<sub>2</sub> and the metallic 1T-MoS<sub>2</sub> and MoO<sub>2</sub> phonon modes, whose 3d<sub>5/2</sub> and 3d<sub>3/2</sub> binding energies (BEs) were 229.0 and 232.2 eV for the 2H phase [46], 228.5 and 231.7 eV for 1T-MoS<sub>2</sub> [13], and 230.4 and 233.6 eV for MoO<sub>2</sub> [13,47], respectively, with the most intensive peaks for the thermodynamically metastable 1T-MoO<sub>2</sub>. A similar conclusion can be drawn from the analysis of S 2p BE peaks presented in Figure 4c. For this spectrum, the doublets with components at 161.5 and 162.6 eV correspond to the BEs of S 2p<sub>3/2</sub> and 2p<sub>1/2</sub> states in the 2H-MoS<sub>2</sub>, whereas the most intense peaks are characteristic of the octahedral 1T phase. It is worth noticing that some amounts of Mo<sup>6+</sup> and S<sup>4+</sup> were also determined, for which the binding energies of 232.5 eV and 235.6 eV (Mo 3d<sub>5/2</sub> and Mo 3d<sub>3/2</sub>, respectively), were attributed to MoO<sub>3</sub>, and 168.4 and 169.6 eV (S 2p<sub>3/2</sub> and S 2p<sub>1/2</sub>, respectively) to SO<sub>2</sub> [48]. The analysis of Mo 3p and C 1s modes also revealed the presence of nitrogen and carbon (Figure 4d,) in the hybrid film synthesized with L-cysteine, indicating the formation of multiphase 1T/2H-MoS<sub>2</sub>-MoO<sub>x</sub>/C,N material. With regard to the N 1s spectrum, the peak located at 401.6 eV should be ascribed to the intercalation of NH<sub>4</sub><sup>+</sup>, whereas the BE peaked at 397.0 eV can be attributed to the formation of Mo-N bond. From the XPS analysis, the concentration of elements was C, Mo, S, O, and N equalled to 32.8 at.% for C, 11.5 at.% for Mo, 25.3 at.% for S, 26.4 at.% for O, and 4.0 at.% for N.

The interactions between various amino acids (AA) and single-layer MoS<sub>2</sub> nanosheet have been theoretically investigated by Dong et al. [49], concluding that no chemical bonds formed between them. The adsorption strength of AA on MoS<sub>2</sub> depended on the AA type influencing the spatial distribution of the HOMO and LUMO orbitals and the MoS<sub>2</sub> band gap decreased. As reported by Dong et al., the cysteine adsorption at the single layer 2H-MoS<sub>2</sub> substrate reduced the band gap by 0.27 eV because of the enhanced hybridization between the Mo d-orbital and the S p-orbital after oxygen incorporation [49]. Therefore, it is reasonable to suggest that adsorption of cysteine at the nanosheets surface of the hybrid multiple-layered MoS<sub>2</sub> film could modulate its catalytic properties towards becoming more active and stable. However, we did not determine the insertion of cysteine molecules, although the XP spectra revealed insertion of C and N atoms inside the MoS<sub>2</sub>-cyst products. Since cysteine molecules start degrading at around 200 °C, the formation and insertion of MoS<sub>2</sub> fragments at 220 °C may be expected. The insertion of guest species, as shown in the study, was also elucidated by the greatly disrupted S-Mo-S layers and the increased distance between two neighboring ones (see Figure 1c). We suggest that insertion of guest species may affect the catalytic stability and activity of 1T-/2H-MoS<sub>2</sub>/MoO<sub>x</sub> hybrid films because of the formation of a higher amount of catalytically active sites and the stabilization of the highly conducting 1T-MoS<sub>2</sub> phase. The low Tafel slope determined for this HER

electrocatalyst ( $32.6 \text{ mV dec}^{-1}$ ), which is much smaller than that of the bulk  $\text{MoS}_2$ , could be explained as follows.

According to Weiss et al. [50], the thermal degradation of cysteine molecules proceeds via this reaction:



The pathway to the formation of  $\text{C}_4\text{H}_7\text{N}$  could be the ejection of the carboxyl group,  $-\text{C}^*\text{OOH}$ , and the  $-\text{SH}$  group from Cyst. The remaining chain  $\text{NH}_2-\text{C}_\alpha-\text{C}^*$  is short, but still suitable for intercalation, further cyclization, and formation of 2,5-dihydro-1H-pyrrole (ChemSpider 13870958) with 69 Da or another pyrrole with the double bond elsewhere in the ring. The exact composition of the intercalated species has not been elucidated yet. However, if intercalated cysteine fragments are like  $\text{NH}_2-\text{C}_\alpha-\text{C}^*$ , the processing of HER at the  $\text{MoS}_2/\text{NH}_2-\text{C}_\alpha-\text{C}^*$  edges may be changed significantly towards a reaction with a low Tafel slope, as established in this study. Further studies are currently being carried out by Fourier-transformed infrared (FTIR) spectroscopy and nuclear magnetic resonance (NMR).

### 3. Conclusions

Here, we report on the one-pot hydrothermal synthesis of the hybrid-type 2D  $\text{MoS}_2$ -based electrocatalyst for efficient hydrogen evolution from the acidic solution. Based on the XPS, SEM, HRTEM, and TG results it was inferred that the increased activity and stability of a novel hybrid  $\text{MoS}_2$  film are related to the formation of a 2D composite from dominating metallic-type and highly active 1T- $\text{MoS}_2$  and  $\text{MoO}_2$  phases interfaced with the semiconducting 2H- $\text{MoS}_2$  and  $\text{MoO}_3$  phases and carbon. The surprisingly low Tafel slope of  $32.6 \text{ mV dec}^{-1}$  for this HER electrocatalyst in the strongly acidic aqueous solution was determined for the first time implying that  $\text{H}_2$  formation at this electrode proceeds via the Volmer–Tafel pathway. This was attributed to the possible insertion between two neighboring S–Mo–S nanosheets of thermally degraded cysteine residue species, like  $\text{NH}_2-\text{C}_\alpha-\text{C}^*$ . These findings highlight the need to study further the influence of amino acid on the formation mechanism of hybrid films.

### 4. Materials and Methods

#### 4.1. Materials and Chemicals

Ammonium heptamolybdate tetrahydrate ( $(\text{NH}_4)_6\text{Mo}_7\text{O}_{24} \cdot 4\text{H}_2\text{O}$  (99.5%)) was obtained from Rechem (Bratislava, Slovakia), whereas thiourea,  $(\text{NH}_2)_2\text{CS}$  (99%), and L-cysteine were purchased from Sigma-Aldrich (St. Louis, MO, USA) and used as received. The Ti specimens with the working surface of  $1.0 \text{ cm}^2$  ( $7 \times 7 \text{ mm}^2$ ) and a tag ( $1 \times 30 \text{ mm}^2$ ) were cut from Ti foil (99.7 at%, 0.127 mm thick, Aldrich). For Ti surface anodizing,  $\text{NH}_4\text{F}$  and  $\text{H}_3\text{PO}_4$  were purchased from Rechem, Bratislava, Slovakia. Aqueous solution for hydrogen evolution was prepared from deionized water (18.4 M $\Omega$ ) and analytically grade sulfuric acid.

#### 4.2. Ti Surface Preparation and Anodizing

The surface of samples was ultrasonically cleaned in acetone, ethanol, and water (6 min in each) and air dried. Ti samples anodizing was conducted in the thermostated Teflon cell containing  $2.0 \text{ mol L}^{-1} \text{ H}_3\text{PO}_4$  and  $0.5 \text{ mol L}^{-1}$  of  $\text{NH}_4\text{F}$  at  $17 \pm 0.3 \text{ }^\circ\text{C}$  and 20 V for 1 h. Two platinum plates were used as cathodes. After anodizing, the specimens were thoroughly rinsed, air-dried, and calcined at  $450 \text{ }^\circ\text{C}$  for 2 h using a  $10 \text{ }^\circ\text{C min}^{-1}$  ramp. An anatase  $\text{TiO}_2$  nanotubed sublayer between Ti and  $\text{MoS}_2$  was chosen as the substrate for the nanostructured HER catalyst because of its fairly good chemical and thermal stability, huge surface area, low resistance in the hydrogen environment, and because of the adsorption affinity of the  $\text{MoS}_2$  species to titanium oxide [51,52].



#### 4.3. Synthesis

To cover the Ti/TiO<sub>2</sub> samples with catalytically active nanostructured MoS<sub>2</sub> film, the hydrothermal processing was conducted in a Teflon lined stainless steel autoclave (25 mL in volume) at 220 °C for 5 to 10 h using a 10 °C min<sup>-1</sup> ramp. An aqueous solution of 5 mmol L<sup>-1</sup> ammonium heptamolybdate and 90 mmol L<sup>-1</sup> thiourea without and containing up to 5 mmol L<sup>-1</sup> of L-cysteine was used. The synthesized products were collected by centrifugation, rinsed thoroughly, and dried at 60 °C. To obtain densely packed MoS<sub>2</sub> nanoplatelet films well-attached to the substrate, the Ti specimen covered with the nanotubed anatase TiO<sub>2</sub> layer in a thickness of about 1 µm was inserted inside the reactor.

#### 4.4. Raman Spectra

Raman investigations were performed on an inVia (Renishaw, New Mills, UK) spectrometer equipped with a thermoelectrically cooled (−70 °C) CCD camera. Spectra were excited at 532 nm by a diode-pumped solid-state laser on a ~2 µm diameter spot with power at the sample = 0.06 mW. The accumulation time was 400 s. Raman scattering wavenumber axis was calibrated by the silicon peak at 520.7 nm. To determine the parameters of the bands, the fitting of experimental spectra with the Gaussian–Lorentzian shape components using GRAMS/A1 8.0 (Thermo Scientific) software (version 8.0, Thermo Electron Corp.) was conducted.

#### 4.5. SEM and HRTEM

The morphology and microstructure of the films and species obtained were analyzed using a scanning electron microscope (FEI Helios Nanolab 650, Eindhoven, The Netherlands) and a high-resolution transmission microscope FEI TECNAI F20 (Eindhoven, The Netherlands). To estimate their elemental composition, the products were analysed with a CrossBeam Auriga Workstation (Eindhoven, The Netherlands) equipped with a field emission gun and an energy dispersive X-ray spectrometer.

#### 4.6. XPS

X-ray photoelectron spectroscopy (XPS) was used to evaluate the relative elemental composition of the samples. For the XPS measurements, a spectroscopy VERSAPROBE PHI 500 from Physical Electronics (Physical Electronics, Chanhassen, MN, USA) was used; the excitation source was a monochromatized AlK. The energy resolution was 0.6 eV. A dual-beam charge neutralization (electron gun (~1 eV) and Argon Ion gun (<10 eV)) was used for charge compensation. The C1s peak at 284.3 eV was used for binding energy calibration.

#### 4.7. TG/HDSC-MS

A simultaneous thermal analysis STA Pt 1600 (Linseis, Germany) apparatus equipped with a mass spectrometer MS Thermostar GDS 320 (Linseis/Pfeiffer, Germany) was used for research on the thermal decomposition processes of L-cysteine. For this, the specimen of 10 mg weight in PtRh cans was evacuated and then heated at 10 °C min<sup>-1</sup> in an argon atmosphere. The data were collected and fitted using the Evaluation and Quadera software (version 4.62, INFICON AG, Bad Ragaz, Switzerland).

#### 4.8. Cyclic Voltammetry

Electrochemical measurements were performed in a three-electrode-configured setup using a Zahner Zennium (Kronach, Germany) electrochemical workstation. The (Ag/AgCl, KCl<sub>sat</sub>) electrode was used as a reference, while a glassy carbon stripe with an area of ~10 cm<sup>-2</sup> and Ti/TiO<sub>2</sub>/MoS<sub>2</sub> were used as the counter and the working electrode, respectively. A linear sweep voltammetry with a scan rate of 10 mV s<sup>-1</sup> within 0.05 to −0.35 V vs. the RHE potential range was conducted in 0.5 mol L<sup>-1</sup> of H<sub>2</sub>SO<sub>4</sub> pre-purged with H<sub>2</sub> for 30 min. In the stability tests, up to 2000 cycles were recorded. All potentials in the text refer to RHE.

**Author Contributions:** Conceptualization, administration and writing, A.J.; syntheses and electrochemical studies, P.G.; XPS investigations and data analysis, C.B.; TG/DTA/MS study and editing, V.K. All authors have read and agreed to the published version of the manuscript.

**Funding:** CB thanks the Belgian Fund for Scientific Research under the FRFC contract CDR J001019.

**Institutional Review Board Statement:** Not applicable.

**Informed Consent Statement:** Not applicable.

**Data Availability Statement:** Not applicable.

**Acknowledgments:** The authors thank Romualdas Trusovas for Raman spectra collection, Arnas Naujokaitis for SEM images, and Marija Kurtinaitiene for Ti sample preparation. CB thanks the Belgian Fund for Scientific Research under the FRFC contract CDR J001019.

**Conflicts of Interest:** The authors declare no conflict of interest.

## References

1. Sheng, W. Correlating hydrogen oxidation and evolution activity on platinum at different pH with measured hydrogen binding energy. *Nat. Commun.* **2015**, *6*, 5848. [[CrossRef](#)]
2. Sarkar, D.; Liu, W.; Xie, W.; Anselmo, A.C.; Mitragotri, S.; Banerjee, K. MoS<sub>2</sub> field-effect transistor for next-generation label-free biosensors. *ACS Nano* **2014**, *8*, 3992–4003. [[CrossRef](#)] [[PubMed](#)]
3. Shimazu, Y.; Tashiro, M.; Sonobe, S.; Takahashi, M. Environmental effect on hysteresis of transfer characteristics in molybdenum disulfide field effect transistors. *Sci. Rep.* **2016**, *6*, 30084. [[CrossRef](#)] [[PubMed](#)]
4. Ikram, M.; Liu, Y.; Lv, H.; Liu, L.; Rehman, A.U.; Kan, K.; Zhang, W.; He, L.; Wang, Y.; Wang, R.; et al. 3D-multilayer MoS<sub>2</sub> nanosheets vertically grown on highly mesoporous cubic In<sub>2</sub>O<sub>3</sub> for high-performance gas sensing at room temperature. *Appl. Surf. Sci.* **2019**, *466*, 1–11. [[CrossRef](#)]
5. Wang, Z.; Mi, B. Environmental applications of 2D molybdenum disulfide (MoS<sub>2</sub>). *Environ. Sci. Technol.* **2017**, *51*, 8229–8244. [[CrossRef](#)] [[PubMed](#)]
6. Zoller, F.; Luxa, J.; Bein, T.; Fattakhova-Rohlfing, D.; Bouša, D.; Sofer, Z. Flexible freestanding MoS<sub>2</sub>-based composite paper for energy conversion and storage. *Beilstein J. Nanotechnol.* **2019**, *10*, 1488–1496. [[CrossRef](#)]
7. Youn, D.H.; Jang, J.W.; Kim, J.Y.; Jang, J.S.; Choi, S.H.; Lee, J.S. Fabrication of graphene-based electrode in less than a minute through hybrid microwave annealing. *Sci. Rep.* **2015**, *4*, 5492. [[CrossRef](#)] [[PubMed](#)]
8. Li, G.; Zhang, D.; Qiao, Q.; Yu, Y.; Peterson, D.; Zafar, A.; Kumar, R.; Curtarolo, S.; Hunte, F.; Shannon, S.; et al. All the Catalytic Active Sites of MoS<sub>2</sub> for Hydrogen Evolution. *J. Am. Chem. Soc.* **2016**, *138*, 16632–16638. [[CrossRef](#)]
9. Li, H.; Tsai, C.; Koh, A.L.; Cai, L.; Contryman, A.W.; Fragapane, A.H.; Zhao, J.; Han, H.S.; Manoharan, H.C.; Abild-Pedersen, F.; et al. Activating and Optimizing MoS<sub>2</sub> Basal Planes for Hydrogen Evolution through the Formation of Strained Sulphur Vacancies. *Nat. Mater.* **2016**, *15*, 48–53. [[CrossRef](#)]
10. Voiry, D.; Fullon, R.; Yang, J.; Silva, C.C.L.; Kappera, R.; Buzkurt, I.; Kaplan, D.; Lagos, M.J.; Batson, P.E.; Gupta, G.; et al. The role of electronic coupling between substrate and 2D MoS<sub>2</sub> nanosheets in electrocatalytic production of hydrogen. *Nat. Mater.* **2016**, *15*, 1003–1009. [[CrossRef](#)]
11. Li, R.; Yang, L.; Xiong, T.; Wu, Y.; Cao, L.; Yuan, D.; Zhou, W. Nitrogen doped MoS<sub>2</sub> nanosheets synthesized via a low-temperature process as electrocatalysts with enhanced activity for hydrogen evolution reaction. *J. Power Source* **2017**, *356*, 133–139. [[CrossRef](#)]
12. Tan, C.; Luo, Z.; Chaturvedi, A.; Cai, Y.; Du, Y.; Gong, Y.; Huang, Y.; Lai, Z.; Zhang, X. Preparation of high-percentage 1T-phase transition metal dichalcogenide nanodots for electrochemical hydrogen evolution. *Adv. Mater.* **2018**, *30*, 1705509. [[CrossRef](#)]
13. Voiry, D.; Mohite, A.; Chhowalla, M. Phase engineering of transition metal dichalcogenides. *Chem. Soc. Rev.* **2015**, *44*, 2702–2712. [[CrossRef](#)]
14. Huang, W.Z.; Xu, Z.D.; Liu, R.; Zheng, Y.F. Tungstenic acid induced assembly of hierarchical flower-like MoS<sub>2</sub> spheres. *Mater. Res. Bull.* **2008**, *43*, 2799–2805. [[CrossRef](#)]
15. Naujokaitis, A.; Gaigalas, P.; Bittencourt, C.; Mickevičius, S.; Jagminas, A. 1T/2H MoS<sub>2</sub>/MoO<sub>3</sub> hybrid assemblies with glycine as highly efficient and stable electrocatalyst for water splitting. *Int. J. Hydrog. Energy* **2019**, *44*, 24237–24245. [[CrossRef](#)]
16. Jagminas, A.; Naujokaitis, A.; Žalneravičius, R.; Jasulaitiene, V.; Valušis, G. Tuning the activity of nanoplatelet MoS<sub>2</sub>-based catalyst for efficient hydrogen evolution via electrochemical decoration with Pt nanoparticles. *Appl. Surf. Sci.* **2016**, *385*, 56–62. [[CrossRef](#)]
17. Huang, X.; Zeng, Z.; Bao, S.; Wang, M.; Qi, X.; Fan, Z.; Zhang, H. Solution-phase epitaxial growth of noble metal nanostructures on dispersible single-layer molybdenum disulfide nanosheets. *Nat. Commun.* **2013**, *4*, 1444. [[CrossRef](#)] [[PubMed](#)]
18. Peto, J.; Ollar, T.; Vancso, P.; Popov, Z.; Magda, G.Z.; Dobrik, G.; Hwang, C.; Sorokin, P.B.; Tapaszto, N. Spontaneous Doping of the Basal Plane of MoS<sub>2</sub> Single Layers through Oxygen Substitution under Ambient Conditions. *Nat. Chem.* **2018**, *10*, 1246–1251. [[CrossRef](#)] [[PubMed](#)]
19. Lukowski, M.A.; Daniel, A.S.; Meng, F.; Forticaux, A.; Li, L.; Jin, S. Enhanced Hydrogen Evolution Catalysis from Chemically Exfoliated Metallic MoS<sub>2</sub> Nanosheets. *J. Am. Chem. Soc.* **2013**, *135*, 10274–10277. [[CrossRef](#)]

20. Zhang, K.; Kim, H.-J.; Shi, X.; Lee, J.-T.; Choi, J.-M.; Song, M.-S.; Park, J.H. Graphene/acid co-assisted synthesis of ultrathin MoS<sub>2</sub> nanosheets with outstanding rate capability for lithium battery anode. *Inorg. Chem.* **2013**, *52*, 9807–9812. [[CrossRef](#)] [[PubMed](#)]
21. Zhang, K.; Kim, H.-J.; Lee, J.-T.; Chang, G.-W.; Shi, X.; Kim, W.; Ma, M.; Kong, K.-j.; Choi, J.-M.; Song, M.S.; et al. Unconventional pore and defect generation in molybdenum disulfide: Application in high-rate lithium-ion batteries and the hydrogen evolution reaction. *ChemSusChem* **2014**, *7*, 2489–2495. [[CrossRef](#)]
22. Yan, Y.; Ge, X.M.; Liu, Z.L.; Wang, J.Y.; Lee, J.M.; Wang, X. Facile synthesis of low crystalline MoS<sub>2</sub> nanosheet-coated CNT for enhanced hydrogen evolution reaction. *Nanoscale* **2013**, *5*, 7768–7771. [[CrossRef](#)]
23. Hu, J.J.; Zabinski, J.S.; Sanders, J.H.; Bultman, J.E.; Voevodin, A.A. Pulsed Laser Syntheses of Layer-Structured WS<sub>2</sub> Nanomaterials in Water. *J. Phys. Chem. B* **2006**, *110*, 8914–8916. [[CrossRef](#)] [[PubMed](#)]
24. Zelenski, C.M.; Dorhout, P.K. Template Synthesis of Near-Monodisperse<sup>1</sup> Microscale Nanofibers and Nanotubules of MoS<sub>2</sub>. *J. Am. Chem. Soc.* **1998**, *120*, 734–742. [[CrossRef](#)]
25. Feldman, Y.; Wasserman, E.; Szolovitz, D.J.; Tenal, R. High-rate, gas phase growth of MoS<sub>2</sub> nested inorganic fullerenes and nanotubes. *Science* **1995**, *267*, 222–225. [[CrossRef](#)] [[PubMed](#)]
26. Ellmer, K.; Mientus, R.; Seegers, S.; Wei, V. Highly (001)-textured WS<sub>2-x</sub> films prepared by reactive radio frequency magnetron sputtering. *Phys. Status Solidi A* **2004**, *201*, R97–R100. [[CrossRef](#)]
27. Wei, R.; Yang, H.; Du, K.; Fu, W.; Zou, G. A facile method to prepare MoS<sub>2</sub> with nanoflower-like morphology. *Mater. Chem. Phys.* **2008**, *108*, 188–191. [[CrossRef](#)]
28. Ma, L.; Chen, W.X.; Li, H.; Xu, Z.D. Synthesis and characterization of MoS<sub>2</sub> nanostructures with different morphologies via an ionic liquid-assisted hydrothermal rout. *Mater. Chem. Phys.* **2009**, *116*, 400–405. [[CrossRef](#)]
29. Liao, L.; Zhu, J.; Bian, X.; Zhu, L.; Scanlon, M.D.; Girault, H.H. MoS<sub>2</sub> formed on mesoporous graphene as a highly active catalyst for hydrogen evolution. *Adv. Funct. Mater.* **2013**, *23*, 5326–5333. [[CrossRef](#)]
30. Li, X.; Wang, H.; Xie, L.; Liang, Y.; Hong, G.; Dai, H. MoS<sub>2</sub> nanoparticles grown on graphene: An advanced catalyst for the hydrogen evolution reaction. *J. Am. Chem. Soc.* **2011**, *133*, 7296–7299. [[CrossRef](#)]
31. Li, F.; Zhang, L.; Lin, X.; Li, R.; Li, X.; Fang, Y.; Huang, J. Synthesis of CuMoS<sub>2</sub>/rGO hybrid as non-noble metal electrocatalysts for the hydrogen evolution reaction. *J. Power Sources* **2015**, *292*, 15–22. [[CrossRef](#)]
32. Deng, J.; Li, H.; Wang, S.; Ding, D.; Chen, M.; Liu, C.; Tian, Z.; Novoselov, K.S.; Ma, C.; Deng, D.; et al. Multiscale structural and electronic control of molybdenum disulfide foam for highly efficient hydrogen production. *Nat. Commun.* **2017**, *8*, 14430.
33. Li, D.J.; Maiti, U.N.; Lim, J.; Choi, D.S.; Lee, W.J.; Oh, Y.; Lee, G.Y.; So, K. Molybdenum Sulfide/N-Doped CNT Forest Hybrid Catalysts for High-Performance Hydrogen Evolution Reaction. *Nano Lett* **2014**, *14*, 1228–1233. [[CrossRef](#)] [[PubMed](#)]
34. Yu, H.; Yu, X.; Chen, Y.; Zhang, S.; Gao, P.; Li, C. A strategy to synergistically increase the number of active edge sites and the conductivity of MoS<sub>2</sub> nanosheets for hydrogen evolution. *Nanoscale* **2015**, *7*, 8731–8738. [[CrossRef](#)] [[PubMed](#)]
35. Wang, D.; Zhang, X.; Bao, S.; Zhang, Z.; Fei, H. Phase engineering of multiphasic 1T/2H MoS<sub>2</sub> catalyst for highly efficient hydrogen evolution. *J. Mater. Chem. A* **2017**, *5*, 2681–2687. [[CrossRef](#)]
36. Kwak, J.H.; Kwon, I.S.; Abbas, H.G.; Jung, G.; Lee, Y.; Park, J.; Kang, H.S. Stable methylammonium-intercalated 1T-MoS<sub>2</sub> for efficient electrocatalytic hydrogen evolution. *J. Mater. Chem. A* **2018**, *6*, 5613–5617. [[CrossRef](#)]
37. Jaramillo, T.F.; Jorgensen, K.P.; Bonde, J.; Nilsen, J.H.; Horch, S.; Chorkendorff, I.; Norskov, J.K. Identification of Active Edge Sites for Electrochemical H<sub>2</sub> Evolution from MoS<sub>2</sub> Nanocatalysts. *Science* **2007**, *317*, 100–102. [[CrossRef](#)]
38. Kibsgaard, J.; Chen, Z.B.; Reinecke, B.N.; Jaramillo, T.F. Engineering the surface structure of MoS<sub>2</sub> to preferentially expose active edge sites for electrocatalysis. *Nat. Mater.* **2012**, *11*, 963–969. [[CrossRef](#)]
39. Wang, L.; Li, Q.; Xu, H.; Dahl-Petersen, C.; Yang, Q.; Cheng, D.; Cao, D.; Besenbacher, F.; Lauritsen, J.V.; Helveg, S.; et al. Controllable etching of MoS<sub>2</sub> basal planes for enhanced hydrogen evolution through the formation of active edge sites. *Nano Energy* **2018**, *49*, 634–643. [[CrossRef](#)]
40. Xie, J.; Zhang, H.; Li, S.; Wang, R.; Sun, X.; Zhou, M.; Zhou, J.; Lou, X.W.; Xie, Y. Defect-rich MoS<sub>2</sub> ultrathin nanosheets with additional active edge sites for enhanced electrocatalytic hydrogen evolution. *Adv. Mater.* **2013**, *25*, 5807–5813. [[CrossRef](#)]
41. Park, S.; Park, J.; Abroshan, H.; Zhang, J.; Guo, J.; Siahrostami, S.; Zheng, X. Enhancing catalytic activity of MoS<sub>2</sub> based plane S-vacancy by Co cluster addition. *ACS Energy Lett.* **2018**, *3*, 2685–2693. [[CrossRef](#)]
42. Qiao, W.; Yan, S.; Song, X.; Zhang, X.; Sun, Y.; Chen, X.; Zhong, W.; Du, Y. Monolayer MoS<sub>2</sub> quantum dots as catalysts for efficient hydrogen evolution. *RSC Adv.* **2015**, *5*, 97696–97701. [[CrossRef](#)]
43. Song, I.; Park, C.; Choi, H.C. Synthesis and properties of molybdenum disulphide: From bulk to atomic layers. *RSC Adv.* **2015**, *2*, 7495–74514. [[CrossRef](#)]
44. Xie, J.; Zhang, J.; Li, S.; Grote, F.; Zhang, X.; Wang, R.; Lei, Y.; Pan, B.; Xie, Y. Controllable Disordered Engineering in Oxygen-Incorporated MoS<sub>2</sub> Ultrathin Nanosheets for Efficient Hydrogen Evolution. *J. Am. Chem. Soc.* **2013**, *135*, 17881–17888. [[CrossRef](#)]
45. Watzele, S.; Fichtner, J.; Garlyyev, B.; Schwammlein, J.N.; Bandarenka, A.S. On the dominating mechanism of the hydrogen evolution reaction of polycrystalline Pt electrodes in acidic media. *ACS Cat.* **2018**, *8*, 9456–9462. [[CrossRef](#)]
46. Eda, G.; Yamaguchi, J.; Voiry, D.; Fujita, T.; Chen, M.; Chhowalla, M. Photoluminescence from Chemically Exfoliated MoS<sub>2</sub>. *Nano Lett.* **2011**, *11*, 5111–5116. [[CrossRef](#)]
47. Xie, S.; Chen, K.; Bell, A.T.; Iglesia, E. Structural characterization of molybdenum oxide supported on zirconia. *J. Phys. Chem. B* **2000**, *104*, 10059–10068. [[CrossRef](#)]

48. Ahn, C.; Lee, J.; Kim, H.U.; Bak, H.; Jeon, M.; Ryn, G.H.; Lee, Z.; Yeom, G.Y.; Kim, K.; Jang, J. Lower temperature synthesis of large-scale molybdenum disulfide films directly on a plastic substrate. *Adv. Mater.* **2015**, *27*, 5223–5229. [[CrossRef](#)]
49. Zhang, P.; Wang, Z.; Liu, L.; Klausen, L.H.; Wang, Y.; Mi, J.; Dong, M. Modulation the electronic property of 2D monolayer MoS<sub>2</sub> by amino acid. *Appl. Mater. Today* **2019**, *14*, 151–158. [[CrossRef](#)]
50. Weis, I.M.; Muth, C.; Drumm, R.; Kirchner, O.K. Thermal decomposition of the amino acids glycine, cysteine, aspartic acid, asparagine, glutamic acid glutamine, arginine and histidine. *BMC Biophys.* **2018**, *11*, 2. [[CrossRef](#)] [[PubMed](#)]
51. Chen, G.; Song, X.; Guan, L.; Chai, J.; Zhang, H.; Wang, S.; Pan, J.; Tao, J. Defect assisted coupling of MoS<sub>2</sub>/TiO<sub>2</sub> interface and tuning of its electronic structure. *Nanotechnology* **2016**, *27*, 355203. [[CrossRef](#)] [[PubMed](#)]
52. Jagminas, A.; Naujokaitis, A.; Gaigalas, P.; Ramanavičius, S.; Kurtinaitienė, M.; Trusovas, R. Substrate Impact on the Structure and Electrocatalyst Properties of Molybdenum Disulfide for HER from Water. *Metals* **2020**, *10*, 1251. [[CrossRef](#)]